

Adaptive Graduated Nonconvexity Loss

Kyungmin Jung, Thomas Hitchcox, and James Richard Forbes

Abstract—Many problems in robotics, such as estimating the state from noisy sensor data or aligning two LiDAR point clouds, can be posed and solved as least-squares problems. Unfortunately, vanilla nonminimal solvers for least-squares problems are notoriously sensitive to outliers. As such, various robust loss functions have been proposed to reduce the sensitivity to outliers. Examples of loss functions include pseudo-Huber, Cauchy, and Geman-McClure. Recently, these loss functions have been generalized into a single loss function that enables the best loss function to be found adaptively based on the distribution of the residuals. However, even with the generalized robust loss function, most nonminimal solvers can only be solved locally given a prior state estimate due to the nonconvexity of the problem. The first contribution of this paper is to combine graduated nonconvexity (GNC) with the generalized robust loss function to solve least-squares problems without a prior state estimate and without the need to specify a loss function. Moreover, existing loss functions, including the generalized loss function, are based on Gaussian-like distribution. However, residuals are often defined as the squared norm of a multivariate error and distributed in a Chi-like fashion. The second contribution of this paper is to apply a norm-aware adaptive robust loss function within a GNC framework. This leads to additional robustness when compared with state-of-the-art methods. Simulations and experiments demonstrate that the proposed approach is more robust and yields faster convergence times compared to other GNC formulations.

Index Terms—Graduated nonconvexity, robust loss function, least-squares optimization, state estimation.

I. INTRODUCTION

LEAST squares problems appear in robotics, computer vision, and data analytics. However, traditional least-squares solvers perform poorly in the presence of *outliers* that are often caused by spurious sensor data, faulty data association, and model misspecification [1]. To reduce the sensitivity to outliers during minimization of a least-squares objective function, *robust loss functions* (RLFs), such as pseudo-Huber [2], Cauchy [3], and Geman-McClure [4], have been proposed. However, the main drawback of these RLFs is that they must be hand-picked and manually tuned a priori without knowledge of the actual residual distribution.

A generalized loss function capable of adapting to the actual residual distribution was presented in [5] where it was shown to represent a superset of many common RLFs. A single continuous-valued hyperparameter in the loss function can be set such that the function is adjusted to model a wider family

This work was supported in part by Voyis Imaging Inc. through the Natural Sciences and Engineering Research Council of Canada (NSERC) Collaborative Research and Development (CRD) Program, the NSERC Discovery Grant program, and in part by the McGill Engineering Doctoral Award (MEDA) Program at McGill University.

Kyungmin Jung, Thomas Hitchcox, and James Richard Forbes are with the Department of Mechanical Engineering, McGill University, Montreal, QC, Canada, H3A 0C3. kyungmin.jung@mail.mcgill.ca, thomas.hitchcox@mail.mcgill.ca, james.richard.forbes@mail.mcgill.ca.

of problems and improve flexibility. The adaptive loss function in [5] was originally implemented in computer vision tasks. Later, [5] was extended and applied to general nonlinear least-squares problems in [6] by incorporating the hyperparameter as a part of the estimation process. Also, [6] extended the usable range of this parameter to deal with a larger set of outlier distributions.

Recently, [7] noted that most of the loss functions assume the residuals follow a Gaussian-like distribution with a mode of zero. However, in most nonlinear least-squares problems, the residuals are defined as the norm of a multivariate error, which results in a Chi-like distribution with a nonzero mode. Thus, applying the adaptive loss function directly to the residual distribution may lead to poor weight assignment. This issue was addressed in [7] by finding the mode of the Chi-like distribution and applying the adaptive loss function to the *mode-shifted* residuals. The proposed method, called the adaptive Maxwell-Boltzmann (AMB), was demonstrated in point-cloud alignment and pose averaging, and outperformed other state-of-the-art RLFs.

Nonlinear least-squares problems are difficult to solve *globally* due to the nonconvexity of the objective function [8]. Furthermore, [8] indicated that most of the nonminimal solvers are only able to obtain locally optimal solutions. To address this problem, [8] proposed to combine nonminimal solvers with a method known as graduated nonconvexity (GNC) [9] to solve optimization problems without requiring an initial estimate. GNC and the Black-Rangarajan duality [9] were tailored to traditional loss functions like Geman-McClure (GM) and truncated least-squares (TLS), and used with nonminimal solvers in point-cloud registration, mesh registration, pose-graph optimization, and shape alignment. Although GNC's global optimality cannot be guaranteed, the proposed method was able to solve the aforementioned problems without requiring an initial guess of the state prior to optimization, resulting in a more accurate solution compared to other local solvers.

The primary contribution of this work is a detailed derivation of the adaptive loss function and GNC combination (AGNC). Previously, GNC has been tailored to a specific loss function of choice. However, the combination of GNC with the generalized loss function no longer necessitates the specification of a particular loss function and shows more robustness even with a highly nonconvex objective function. Blending GNC with the generalized loss function is mentioned in [5]. However, the specific derivation, nor its limitations, are discussed.

The secondary contribution of this paper is to acknowledge the Chi-like residual distribution and incorporate GNC into AMB (GNC AMB). Accounting for the mode of the residual distribution is expected to deliver faster convergence rates and more robust performance than AGNC. The proposed methods

are tested against fixed RLFs, adaptive RLFs, and other GNC incorporated loss functions.

The remainder of this paper is organized as follows. Section II reviews concepts such as standard and adaptive RLFs, GNC, and AMB. Section III presents the derivation of the novel AGNC loss function. The proposed methods are applied to a linear-regression problem and a point-cloud alignment problem in Section IV. Finally, the paper is drawn to a close in Section V.

II. PRELIMINARIES

Let $\mathbf{e}_i = \mathbf{e}(\mathbf{y}_i, \mathbf{g}(\mathbf{x}))$ be an error function that quantifies the difference between the i -th measurement \mathbf{y}_i and the expected measurement given a measurement model $\mathbf{g}(\cdot)$ and a state \mathbf{x} . The Mahalanobis distance of the error function is

$$\epsilon_i(\mathbf{y}_i, \mathbf{x}) = \|\mathbf{e}_i\|_{\Sigma_i^{-1}} = \sqrt{\mathbf{e}_i^T \Sigma_i^{-1} \mathbf{e}_i}, \quad (1)$$

where Σ_i is the covariance on the i -th error. For brevity of notation, $\epsilon_i = \epsilon_i(\mathbf{y}_i, \mathbf{x})$.

A. Robust Loss Functions

Consider the following least-squares problem,

$$\mathbf{x}^* = \arg \min_{\mathbf{x} \in \mathcal{X}} \sum_{i=1}^N \frac{1}{2} \epsilon_i^2, \quad (2)$$

where $\mathbf{x} \in \mathcal{X}$ is the state to be estimated and N is the number of measurements. In the presence of outliers, (2) provides a poor estimate of \mathbf{x} . Robust least-squares solvers substitute the quadratic cost in (2) with a loss function $\rho(\cdot)$,

$$\mathbf{x}^* = \arg \min_{\mathbf{x} \in \mathcal{X}} \sum_{i=1}^N \rho(\epsilon_i). \quad (3)$$

Equation 3 can be solved using an iteratively reweighted least-squares (IRLS) framework [10] that solves a sequence of weighted least-squares problems,

$$\mathbf{x}^* = \arg \min_{\mathbf{x} \in \mathcal{X}} \sum_{i=1}^N \frac{1}{2} w_i \epsilon_i^2. \quad (4)$$

The weights w_i in (4) are obtained by equating the gradients of the loss function in (3) and (4) with respect to \mathbf{x} ,

$$\frac{\partial \rho(\epsilon_i)}{\partial \epsilon_i} \frac{\partial \epsilon_i}{\partial \mathbf{x}} = w_i \epsilon_i \frac{\partial \epsilon_i}{\partial \mathbf{x}}, \quad (5a)$$

$$w_i = \frac{1}{\epsilon_i} \frac{\partial \rho(\epsilon_i)}{\partial \epsilon_i}. \quad (5b)$$

This approach allows standard solvers like Gauss-Newton and Levenberg-Marquardt algorithms to solve (3).

B. Black-Rangarajan Duality and Graduated Nonconvexity

Black-Rangarajan duality introduces regularization in (3),

$$\mathbf{x}^*, \mathbf{w}^* = \arg \min_{\mathbf{x} \in \mathcal{X}, w_i \in (0,1]} \sum_{i=1}^N \left(\frac{1}{2} w_i \epsilon_i^2 + \Phi_\rho(w_i) \right), \quad (6)$$

where w_i is the weight associated to i -th measurement, \mathbf{w}^* is the vector form of optimal weights, and the outlier process

function $\Phi_\rho(\cdot)$ defines a penalty on w_i [9]. An appropriate regularization function $\Phi_\rho(\cdot)$ must be found for a particular loss function $\rho(\cdot)$.

Lemma II.1 (Black-Rangarajan Duality). Given a loss function $\rho(\cdot)$, define $\phi(z) := \rho(\sqrt{z})$. If $\phi(z)$ satisfies

$$\lim_{z \rightarrow 0} \phi'(z) = \frac{1}{2}, \quad (7a)$$

$$\lim_{z \rightarrow \infty} \phi'(z) = 0, \quad (7b)$$

$$\phi''(z) < 0, \quad (7c)$$

then there exists an analytical outlier process function $\Phi_\rho(\cdot)$ that can be written as

$$\rho(\epsilon) = \frac{1}{2} w \epsilon^2 + \Phi_\rho(w). \quad (8)$$

The analytical expression of $\Phi_\rho(\cdot)$ is derived in the Appendix A.

This duality regularizes (4) by introducing the additional constraint $\Phi_\rho(\cdot)$. However, the introduction of regularization results in a nonconvex optimization problem. This nonconvexity can be tackled by using GNC [11]. The idea behind GNC is to choose a surrogate function $\rho_\mu(\cdot)$ with a control parameter μ that changes the shape of $\rho(\cdot)$ such that (6) can be rewritten as

$$\mathbf{x}^*, \mathbf{w}^* = \arg \min_{\mathbf{x} \in \mathcal{X}, w_i \in (0,1]} \sum_{i=1}^N \frac{1}{2} w_i \epsilon_i^2 + \Phi_{\rho_\mu}(w_i), \quad (9)$$

where $\Phi_{\rho_\mu}(\cdot)$ is the outlier process function for the surrogate RLF, $\rho_\mu(\cdot)$. The parameter μ allows a convex approximation of $\rho(\cdot)$ to be obtained such that it can be readily minimized. GNC solves the nonconvex problem by gradually increasing the nonconvexity of $\rho_\mu(\cdot)$ during optimization until it recovers the original function. In [8], (9) is solved using IRLS by modifying μ at every iteration.

C. Adaptive Robust Loss

This section discusses the formulation of the adaptive loss function proposed in [5], its limitations, and the solutions to the limitations proposed by [6]. The simplest form of the adaptive loss function is

$$\rho(\epsilon, \alpha) = \frac{|\alpha - 2|}{\alpha} \left(\left(\frac{\epsilon^2}{|\alpha - 2|} + 1 \right)^{\alpha/2} - 1 \right), \quad (10)$$

where $\alpha \in (-\infty, 2]$ is a shape parameter that controls the robustness of the loss. Accounting for singularities, (10) is rewritten in a piecewise function as

$$\rho(\epsilon, \alpha) = \begin{cases} \frac{1}{2} \epsilon^2 & \text{if } \alpha = 2, \\ \log \left(\frac{1}{2} \epsilon^2 + 1 \right) & \text{if } \alpha = 0, \\ 1 - \exp \left(-\frac{1}{2} \epsilon^2 \right) & \text{if } \alpha = -\infty, \\ \frac{|\alpha - 2|}{\alpha} \left(\left(\frac{\epsilon^2}{|\alpha - 2|} + 1 \right)^{\alpha/2} - 1 \right) & \text{otherwise.} \end{cases} \quad (11)$$

In [5], α is treated as an additional unknown parameter to be optimized along with \mathbf{x} in the generalized loss function,

$$\mathbf{x}^*, \alpha^* = \arg \min_{\mathbf{x} \in \mathcal{X}, \alpha \in (-\infty, 2]} \sum_{i=1}^N \rho(\epsilon_i, \alpha). \quad (12)$$

However, naively solving for (12) can result in a trivial solution with some α^* that downweights all the residuals without affecting \mathbf{x} . Thus, [5] avoids this by adding a regularization term derived from the probability distribution,

$$p(\epsilon | \mu_\epsilon, \alpha) = \frac{1}{Z(\alpha)} \exp(-\rho(\epsilon | \mu_\epsilon, \alpha)), \quad (13a)$$

$$Z(\alpha) = \int_{-\infty}^{\infty} \exp(-\rho(\epsilon | \mu_\epsilon, \alpha)) d\epsilon, \quad (13b)$$

where μ_ϵ is the residual mean and $Z(\alpha)$ is a partition function. The general adaptive loss with the regularization term is constructed from the negative log-likelihood of (13a),

$$\rho_a(\epsilon, \alpha) = -\log(p(\epsilon | \mu_\epsilon, \alpha)) \quad (14a)$$

$$= \rho(\epsilon, \alpha) + \log(Z(\alpha)). \quad (14b)$$

However, (14b) is only defined for $\alpha \geq 0$ because $Z(\alpha)$ diverges when $\alpha < 0$.

To solve this issue, [6] computes an approximate partition function $\tilde{Z}(\alpha)$ by limiting the integral bounds with a hyperparameter τ such that

$$\tilde{Z}(\alpha) = \int_{-\tau}^{\tau} \exp(-\rho(\epsilon | \mu_\epsilon, \alpha)) d\epsilon. \quad (15)$$

This allows the shape parameter to be dynamically adapted for values between $-\infty$ and 2. The truncation bound is often set for a specific problem. For example, if the magnitude of the residuals is expected to be large, a larger τ value is used. Further, [6] finds the optimal shape parameter through a grid search by solving the optimization problem

$$\alpha^* = \arg \min_{\alpha \in (-\infty, 2]} -\log(p(\epsilon | \mu_\epsilon, \alpha)) \quad (16a)$$

$$= \arg \min_{\alpha \in (-\infty, 2]} N \log(\tilde{Z}(\alpha)) + \sum_{i=1}^N \rho(\epsilon_i, \alpha). \quad (16b)$$

Having α^* and the loss function (14b), the weights w_i are obtained using (5b),

$$w(\epsilon, \alpha^*) = \begin{cases} 1 & \text{if } \alpha^* = 2, \\ \frac{2}{\epsilon^2 + 2} & \text{if } \alpha^* = 0, \\ \exp(-\frac{1}{2}\epsilon^2) & \text{if } \alpha^* = -\infty, \\ \left(\frac{\epsilon^2}{|\alpha^* - 2|} + 1\right)^{\alpha^*/2 - 1} & \text{otherwise.} \end{cases} \quad (17)$$

D. Adaptive Maxwell-Boltzmann Loss

Residuals are often defined as a squared norm of a multivariate error that follows a Chi distribution with some nonzero peak, $\tilde{\epsilon}$. However, most of the existing RLFs are derived based on Gaussian-like distribution with its peak at zero. Therefore, the residuals will be weighted the highest near zero and weighted less as they get further away from zero. Recently, [7] discovered that this Gaussian assumption results in lower

weights assigned to residuals clustered around the non-zero mode value. As such, [7] proposed the AMB loss function that addresses this problem by first fitting an n_e -dimensional Maxwell-Boltzmann (MB) distribution to the residuals,

$$p_{\text{MB}}(\epsilon | a, n_e) = \frac{\epsilon^{n_e - 1}}{a^{n_e} 2^{(n_e/2 - 1)} \Gamma(n_e/2)} \exp(-\epsilon^2/2a^2), \quad (18)$$

where n_e is the dimension of the residual and a is the MB shape parameter. The optimal shape parameter a^* can be found by minimizing the negative log-likelihood of (18) with respect to a . However, this could result in poor estimation in the presence of outliers. Thus, a^* is found by solving

$$a^* = \arg \min_{a \in \mathbb{R}^+} \int_0^{\tau} (q(\epsilon) \cdot (p_{\text{MB}}(\epsilon | a, n_e) - q(\epsilon)))^2 d\epsilon, \quad (19)$$

where $q(\epsilon)$ is the residual distribution. This results in a better fit in high-frequency inlier areas. Equation (19) is solved analytically using Newton's method with a line search [7]. The optimal shape parameter is used to find the nonzero mode value,

$$\tilde{\epsilon} = a^* \sqrt{n_e - 1}. \quad (20)$$

Residuals satisfying $\epsilon \leq \tilde{\epsilon}$ are considered inliers and assigned a weight equal to 1, and any residuals satisfying $\epsilon > \tilde{\epsilon}$ are assigned a weight that is strictly less than one in an adaptive fashion. To do so, the optimal shape parameter α^* that fits the *mode-shifted* residuals, $\xi = \epsilon - \tilde{\epsilon}$, is computed using (16b)

$$\alpha^* = \arg \min_{\alpha \in (-\infty, 2]} M \log(\tilde{Z}(\alpha)) + \sum_{i=1}^M \rho(\xi_i, \alpha), \quad (21)$$

where M is the total number of ξ_i . The partition function $\tilde{Z}(\cdot)$ is now computed with the *mode-shifted truncation bound*, $\tilde{\tau} = \tau - \tilde{\epsilon}$,

$$\tilde{Z}(\alpha) = \int_0^{\tilde{\tau}} \exp(-\rho(\xi | \mu_\xi, \alpha)) d\xi. \quad (22)$$

Thus, given $\tilde{\epsilon}$ and α^* , the weights are

$$\tilde{w}(\epsilon, \tilde{\epsilon}, \alpha^*) = \begin{cases} 1 & \text{if } \epsilon \leq \tilde{\epsilon}, \\ w(\epsilon - \tilde{\epsilon}, \alpha^*) & \text{if } \epsilon > \tilde{\epsilon}. \end{cases} \quad (23)$$

These weights $w(\cdot)$ in (23) are from (17). A detailed derivation and visualization of the AMB loss function $\rho(\epsilon, \tilde{\epsilon}, \alpha)$ can be found in Appendix B.

III. METHODOLOGY

This section first presents the derivation of the proposed adaptive graduated nonconvexity (AGNC) loss function. Assuming that the optimal shape parameter α^* is precomputed using (16b), GNC is incorporated into (10). Based on the properties inherited from GNC, optimization with the proposed loss function is expected to converge without any prior state estimate. Further, the proposed method is extended to adapt the nonzero peak of the residual distribution by incorporating AMB from [7].

A. GNC Surrogate Function to Adaptive Robust Loss

Suppose there exists a surrogate function of (10) of the form

$$\rho_\mu(\epsilon, \alpha^*) = \frac{|f - 2|}{f} \left(\left(\frac{\epsilon^2}{|f - 2|} + 1 \right)^{f/2} - 1 \right), \quad (24)$$

where $f = f(\mu, \alpha^*)$ is a *shape function* that takes in the optimal shape parameter α^* and the convexity control parameter μ as inputs to determine the shape of the adaptive loss function. Recall that GNC computes a solution to the nonconvex problem by starting from its convex surrogate and gradually increasing its nonconvexity until the original function is recovered. Notice that $\rho_\mu(\cdot)$ becomes quadratic in the limit of $f(\cdot) \rightarrow 2$, and that $\rho(\cdot)$ is recovered in the limit of $f(\cdot) \rightarrow \alpha^*$. Also, $f(\cdot) \leq 2$ for all μ because (10) is only defined for $\alpha \in (-\infty, 2]$. As such, the shape function $f(\cdot)$ must satisfy the conditions,

$$\lim_{\mu \rightarrow c_1} f(\mu, \alpha^*) = 2, \quad (25a)$$

$$\lim_{\mu \rightarrow c_2} f(\mu, \alpha^*) = \alpha^*, \quad (25b)$$

$$f(\mu, \alpha^*) \leq 2. \quad (25c)$$

The parameters c_1 and c_2 are user-defined constants. The choice of c_1 and c_2 determines the shape of $f(\cdot)$.

Examples of c_1 and c_2 , as well as possible shape functions, are presented next.

Example III.1. Let $c_1 = 0$ and $c_2 = \infty$. Amongst others, the shape function $f(\cdot)$ can be formulated as

$$f(\mu, \alpha^*) = \frac{\alpha^* \mu + 2}{\mu + 1}, \quad (26)$$

such that

$$\lim_{\mu \rightarrow 0^+} f(\mu, \alpha^*) = \lim_{\mu \rightarrow 0^+} \frac{\alpha^* \mu + 2}{\mu + 1} = 2, \quad (27a)$$

$$\lim_{\mu \rightarrow \infty} f(\mu, \alpha^*) = \lim_{\mu \rightarrow \infty} \frac{\alpha^* \mu + 2}{\mu + 1} = \alpha^*, \quad (27b)$$

$$f(\mu, \alpha^*) \leq 2, \quad \forall \mu \in \mathbb{R}^+. \quad (27c)$$

However, when $\alpha^* = -\infty$, (27b) is undefined. As such, another shape function is used for $\alpha^* = -\infty$,

$$f(\mu, \alpha^*) = f(\mu) = 2 - \mu, \quad (28)$$

which satisfies

$$\lim_{\mu \rightarrow 0^+} f(\mu) = \lim_{\mu \rightarrow 0^+} 2 - \mu = 2, \quad (29a)$$

$$\lim_{\mu \rightarrow \infty} f(\mu) = \lim_{\mu \rightarrow \infty} 2 - \mu = -\infty. \quad (29b)$$

Thus, with a precomputed α^* , (10) is optimized by increasing μ from 0 to ∞ in this example. This specific example is converged when μ reaches ∞ as the original function is only recovered at $\mu = \infty$, which is impractical. Thus, it is possible to choose some $c_2 > c_1$ that is finite, and derive the corresponding shape function, as discussed next in Example III.2.

Example III.2. Alternatively, the constants can be chosen for decreasing μ . Let $c_1 = \infty$ and $c_2 = 1$ such that the original

function is restored as μ decreases from ∞ to 1. Amongst others, the shape function $f(\cdot)$ can be formulated as

$$f(\mu, \alpha^*) = \frac{\alpha^* + 2\mu - 2}{\mu}, \quad (30)$$

such that

$$\lim_{\mu \rightarrow \infty} f(\mu, \alpha^*) = \lim_{\mu \rightarrow \infty} \frac{\alpha^* + 2\mu - 2}{\mu} = 2, \quad (31a)$$

$$\lim_{\mu \rightarrow 1} f(\mu, \alpha^*) = \lim_{\mu \rightarrow 1} \frac{\alpha^* + 2\mu - 2}{\mu} = \alpha^*, \quad (31b)$$

$$f(\mu, \alpha^*) \leq 2, \quad \forall \mu \in [1, \infty). \quad (31c)$$

Again, for $\alpha^* = -\infty$, (31a) and (31a) are not satisfied. Thus, a different shape function is chosen for such corner case,

$$f(\mu, \alpha) = f(\mu) = \frac{2\mu - 3}{\mu - 1}, \quad (32)$$

which satisfies

$$\lim_{\mu \rightarrow \infty} f(\mu) = \lim_{\mu \rightarrow \infty} \frac{2\mu - 3}{\mu - 1} = 2, \quad (33a)$$

$$\lim_{\mu \rightarrow 1^+} f(\mu) = \lim_{\mu \rightarrow 1^+} \frac{2\mu - 3}{\mu - 1} = -\infty. \quad (33b)$$

B. Adaptive GNC Weight Update

Similar to [8], (9) is optimized using IRLS with changing μ . The states \mathbf{x} and the weights w_i are optimized alternatively and iteratively. Recall that the Mahalanobis distance of the residual is a function of \mathbf{x} . Thus, minimizing (9) with respect to \mathbf{x} and fixed weights w_i results in minimizing (4) because the outlier process function does not depend on \mathbf{x} . On the other hand, minimizing (9) with respect to w_i and fixed $\bar{\mathbf{x}}$ results in

$$\mathbf{w}^* = \arg \min_{w_i \in (0, 1]} \sum_{i=1}^N \frac{1}{2} w_i \epsilon_i(\bar{\mathbf{x}})^2 + \Phi_{\rho_\mu}(w_i). \quad (34)$$

With $\Phi_{\rho_\mu}(\cdot)$ derived in Appendix C, the solution to (34) for changing values of μ is given as

$$w^*(\epsilon, \alpha^*) = \begin{cases} 1 & \text{if } f = 2, \\ \frac{2}{\epsilon^2 + 2} & \text{if } f = 0, \\ \exp(-\frac{1}{2}\epsilon^2) & \text{if } f = -\infty, \\ \left(\frac{\epsilon^2}{|f-2|} + 1\right)^{f/2-1} & \text{otherwise.} \end{cases} \quad (35)$$

C. GNC Algorithm with AMB Loss

Recall that most of the robust loss functions that are subsets of (10) assume a Gaussian-like residual distribution, and this assumption can inadvertently lead to problems with the weighting scheme [7]. Thus, the adaptive GNC loss function is extended to incorporate the “mode gap” approach of [7].

The mode of the residual distribution $\tilde{\epsilon}$ is estimated using (20) by fitting an MB distribution (18) to the residual distribution $q(\epsilon)$ as shown in (19). Having estimated the mode value, the optimal shape parameter for the *mode-shifted* residuals is found using (21) and (22). With a fixed a^* , GNC is applied to the AMB loss function. Implementation of GNC-AMB is shown in Algorithm 1.

Algorithm 1 Implementation of GNC-AMB

Require: $\boldsymbol{\epsilon} = [\epsilon_1 \ \epsilon_2 \ \dots \ \epsilon_N]^\top, \mu$

Ensure: $\epsilon_i = \|\mathbf{e}_i\|_{\Sigma^{-1}}$

Compute a^* of $q(\boldsymbol{\epsilon})$ using (19).

Compute $\tilde{\epsilon}$ using (20).

Compute the *mode-shifted* values

$$\boldsymbol{\xi} = \boldsymbol{\epsilon} - \tilde{\epsilon} \mathbf{1} \text{ and } \tilde{\tau} = \tau - \tilde{\epsilon},$$

where $\mathbf{1}$ is a vector of ones.

Compute α^* of $q(\boldsymbol{\xi})$ using (21) and (22).

Ensure: $\mu | f(\mu, \alpha^*) \rightarrow 2$

while $f \neq \alpha^*$ **do** \triangleright Perform AGNC algorithm over $\boldsymbol{\xi}$

Compute $f(\mu, \alpha^*)$.

Compute the optimal weights \mathbf{w}^* for $\boldsymbol{\xi}$ using (35).

Solve for the states \mathbf{x}^* with \mathbf{w}^* using (4).

Update μ such that $f(\mu, \alpha^*)$ approaches α^* .

end while

IV. RESULTS

The proposed methods, AGNC and GNC-AMB, are tested on a variety of problems including the simple multidimensional linear-regression studied in [8] and a point-cloud alignment. The results are compared against traditional and also recently proposed loss functions [12] including existing GNC-applied loss functions. Traditional loss functions include Cauchy [3], Welsch [13], Barron's adaptive robust loss (BA) [5], Chebrolu *et al.*'s adaptive robust loss (CA) [6], and Hitchcox and Forbes' adaptive MB (AMB) [7]. GNC-applied loss functions include GNC with Geman-McClure (GNC-GM) and GNC with truncated least-squares (GNC-TLS) [8].

A. Linear-Regression Problem

Consider the following problem

$$\mathbf{A}\mathbf{x} = \mathbf{y}, \quad (36)$$

where \mathbf{x} is the state to be estimated and \mathbf{y} are n -dimensional measurements. The noise free measurements, $\bar{\mathbf{y}}$, are corrupted by isotropic Gaussian noise, $\delta\mathbf{y} \sim \mathcal{N}(\mathbf{0}, \Sigma)$, such that $\mathbf{y} = \bar{\mathbf{y}} + \delta\mathbf{y}$. The corresponding error function for the i -th measurement is thus

$$\mathbf{e}(\mathbf{y}_i, \mathbf{x}) = \mathbf{A}_i \mathbf{x} - \mathbf{y}_i. \quad (37)$$

Note that the state \mathbf{x} , the measurement \mathbf{y}_i , and the error \mathbf{e} are all unitless. The residual to this problem is defined according to (1), with the measurement covariance, $\Sigma = \sigma^2 \mathbf{1}$. Some of these measurements are randomly selected and modified as outliers, \mathbf{y}^{out} , that satisfy

$$\|\mathbf{e}(\mathbf{x}, \mathbf{y}_i^{\text{out}})\|_{\Sigma^{-1}}^2 > \chi^2(n, 0.9973), \quad (38)$$

where $\chi^2(n, 0.9973)$ represents the 99.73% probability of the inverse cumulative distribution function of the χ^2 distribution with n degrees of freedom.

For this experiment, 1×10^5 measurements were generated with $n = 3$ and $\sigma = 0.1$. A Monte-Carlo simulation was performed over various proportions of outlier measurements

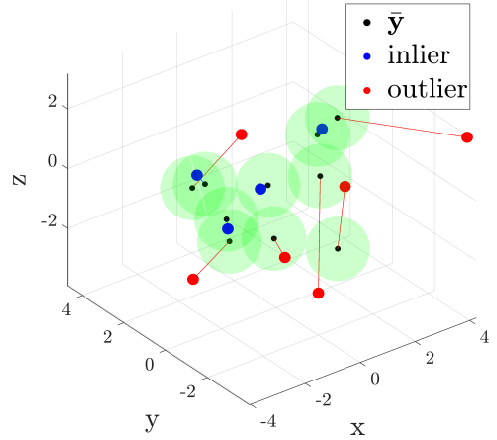


Fig. 1: A visualization of the linear-regression problem with a 60% outlier rate is shown here. Only 10 measurements are shown for clear representation. The locations of the noise-free measurements, $\bar{\mathbf{y}}$, are shown as black dots with their 99.73% confidence bounds displayed as green spheres around each measurement. The noisy inlier and outlier measurements are shown in blue and red dots, respectively, and are connected to the associated noise-free measurement via a red line.

that increased from 20% to 80% in 20% increments. One hundred trials were run at each outlier level, and for each trial, the RLFs were tested for convergence without any prior state estimate. For the loss functions that are based on [6], the truncation bound parameter is set as $\tau = 5$. Figure 1 shows the setup for a single trial with a 60% outlier rate. To obtain the initial residual distribution, $q(\boldsymbol{\epsilon}(\mathbf{y}, \bar{\mathbf{x}}))$, the initial state is obtained using the pseudoinverse of \mathbf{A} .

Overall, GNC-incorporated methods outperform other non-GNC-based loss functions at the expense of longer processing time. For example, AMB, the best-performing method amongst the traditional loss functions in terms of the root mean squared error (RMSE), produces higher errors in all percent outlier levels than any GNC-incorporated method. This behaviour is expected when non-GNC loss functions are optimized without an accurate prior estimate because nonminimal solvers are only able to obtain locally optimal solutions.

Amongst the GNC methods, GNC-TLS produces the lowest RMSE in most of the outlier levels at the cost of considerably high processing time, around 3.5 s per iteration. GNC-AMB follows GNC-TLS in RMSE but with almost 3-fold less processing time. In addition, the proposed method outperforms all other methods in a higher outlier level, for example at 80%, showing more robustness to the high percentage of outliers.

The AGNC method works much better than non-GNC counterparts like BA and CA. However, it is not as robust as GNC-GM to a high outlier percentage. In [5] and [7], it is pointed out that as the percentage of outliers increases, the shape parameter α^* approaches negative infinity, causing the weights assigned to the inlier residuals around the mode $\tilde{\epsilon}$ to be indistinguishable from the weights assigned to the outlier residuals. Thus, GNC-GM, which is equivalent to AGNC with a fixed $\alpha = -2$, performs similarly in a lower number of outliers but performs better in increasing outlier levels.

TABLE I: Results of the linear-regression problem. Error percentiles and processing time for all trials are shown for various methods in different outlier levels. The errors are scaled by a 1×10^3 for readability. For non-GNC methods, only 50% percentile (median) is shown. The lowest error in each column is highlighted in bold for GNC-incorporated RLFs.

	% outliers	Welsch	BA	CA	AMB	GNC-GM	GNC-TLS	AGNC (proposed)	GNC-AMB (proposed)
Error percentiles	20%	4.35	2.79	4.00	1.79	1.28-1.80-2.21	1.15-1.55-1.87	1.35-1.85-2.37	1.19-1.59-1.98
	40%	5.54	3.34	5.00	2.23	1.58-2.01-2.54	1.37-1.81-2.09	1.65-2.19-2.78	1.52-1.88-2.24
	50%-75%-90%	7.12	4.50	6.45	2.83	1.85-2.35-2.94	1.55-2.20-2.63	1.98-2.56-3.13	1.64-2.15-2.75
	80%	8.12	5.70	7.34	3.35	2.77-3.43-4.25	2.71-3.36-4.02	2.88-3.79-4.92	2.59-3.22-3.88
Time (s)	ALL	0.059	0.097	0.096	0.102	1.175	3.473	1.246	1.248

On the other hand, AMB acknowledges the inlier clusters around $\tilde{\epsilon}$ and assigns association weights of $w_i = 1$ to correspondences where $\epsilon_i < \tilde{\epsilon}$. When GNC is incorporated into AMB, the loss function shows more robustness than both AGNC and GNC-GM.

B. Point-Cloud Alignment

Point-cloud alignment (PCA) is an algorithm used to find a 3D rigid transformation that best aligns two input point clouds. The two point clouds are a fixed point cloud, $\mathcal{P} = \{\mathbf{r}_{\ell_1}^{p_i s_1}\}_{i=1}^N$, and a moving point cloud, $\mathcal{Q} = \{\mathbf{r}_{\ell_2}^{q_i s_2}\}_{i=1}^M$. The point measurement $\mathbf{r}_{\ell_1}^{p_i s_1}$ describes the position of the i -th point p_i relative to the position of the sensor s_1 resolved in the sensor frame \mathcal{F}_{ℓ_1} at time t_1 . The relative transformation is represented as an element of matrix Lie group $SE(3)$,

$$\mathbf{T}_{\ell_1 \ell_2}^{s_2 s_1} = \begin{bmatrix} \mathbf{C}_{\ell_1 \ell_2} & \mathbf{r}_{\ell_1}^{s_2 s_1} \\ \mathbf{0} & 1 \end{bmatrix} \in SE(3), \quad (39)$$

where $\mathbf{C} \in SO(3) = \{\mathbf{C} \in \mathbb{R}^{3 \times 3} \mid \mathbf{C}\mathbf{C}^T = \mathbf{1}, \det \mathbf{C} = +1\}$ is the direction cosine matrix that represents the attitude of the laser frame at t_2 with respect to the laser frame at t_1 , and $\mathbf{r}_{\ell_1}^{s_2 s_1} \in \mathbb{R}^3$ represents the position of the sensor at time t_2 relative to the sensor at time t_1 , resolved in the sensor frame at time t_1 . For readability, $\mathbf{T}_{12} = \mathbf{T}_{\ell_1 \ell_2}^{s_2 s_1}$.

The iterative closest point (ICP) algorithm is used to solve a PCA problem herein. The ICP algorithm solves a nonconvex optimization problem, thus it is often solved iteratively from a prior relative transformation $\check{\mathbf{T}}_{12}$. The algorithm first associates each point in \mathcal{P} to its nearest Euclidean neighbour in \mathcal{Q} using $\check{\mathbf{T}}_{12}$. The associated points in \mathcal{Q} are now denoted as $\check{\mathcal{Q}} = \{\mathbf{r}_{\ell_2}^{q_i s_2}\}_{i=1}^N$ where N is the total number of point correspondences. Then, the optimization problem

$$\min_{\mathbf{T}_{12} \in SE(3)} \sum_{i=1}^N \frac{1}{2} w_i \|\mathbf{e}_i(\mathbf{T}_{12}, \mathbf{r}_{\ell_1}^{p_i s_1}, \mathbf{r}_{\ell_2}^{q_i s_2})\|_{\Sigma_i}^2 \quad (40)$$

is solved, where $w_i \in (0, 1]$ are association weights, \mathbf{e}_i are association errors, and Σ_i are association error covariances. Then, the point correspondences are found again with the updated relative transformation. When GNC is applied to the ICP algorithm, the minimization problem in (40) is solved using the GNC algorithm.

1) *Experiment setting*: An open-source point-cloud dataset was used in this experiment [14]. The dataset contains eight point-cloud sequences where each sequence contains ground-truth poses, point-cloud scans, and the overlap ratio between scan pairs. Recall that naively solving (40) can lead to a poor

estimate in the presence of outlier correspondences. Outlier correspondences are frequently found in the case of poor ICP initialization, or when there is a low overlap ratio between \mathcal{P} and \mathcal{Q} . Thus, to thoroughly evaluate the proposed loss functions, ICP performance is evaluated subject to three input settings: the environment diversity, the overlap ratio, and the initial perturbation.

Three point-cloud datasets were chosen from [14], representing a wide range in the diversity of the scanned environment. “ETH Hauptgebaude” (EH) was chosen to represent structured scans, while “Gazebo in Summer” (GZ) and “Mountain Plain” (MP) were chosen to represent semi-structured and unstructured scans, respectively. The “structured” level is a qualitative assessment of the number of geometric primitives visible in the scene. The datasets are shown in Figure 2.

For each point-cloud sequence, two scans are randomly selected to represent \mathcal{P} and \mathcal{Q} , and the selected scan pair is assigned to the corresponding overlap ratio bins. The bins span from 40% to 90% with a bin size of 10%. An example of scan pairs with different overlap ratio is shown in Figure 3.

For each scan pair, three levels of initial relative transformation difficulty are tested: “low,” “medium,” and “high”. The initial relative transformation is computed using $\check{\mathbf{T}}_{12} = \mathbf{T}_{12} \delta \check{\mathbf{T}}$, where \mathbf{T}_{12} is the ground-truth transformation and $\delta \check{\mathbf{T}}$ is the initial perturbation defined in the matrix Lie algebra $\mathfrak{se}(3)$ [15],

$$\log(\delta \check{\mathbf{T}}) = \delta \check{\xi}^\wedge = \begin{bmatrix} \delta \check{\phi} \\ \delta \check{\rho} \end{bmatrix}^\wedge \in \mathfrak{se}(3), \quad (41)$$

where $(\cdot)^\wedge : \mathbb{R}^6 \rightarrow \mathfrak{se}(3)$ is an isometric operator, and $\delta \check{\phi}$ and $\delta \check{\rho}$ represent the perturbation in rotation and translation in $\mathfrak{se}(3)$, respectively. Thus, the perturbation $\delta \check{\mathbf{T}}$ is composed of

$$\delta \check{\phi} \sim \mathcal{N}(\mathbf{0}, \sigma_\phi^2 \mathbf{1}), \quad \delta \check{\rho} \sim \mathcal{N}(\mathbf{0}, \sigma_\rho^2 \mathbf{1}), \quad (42)$$

where σ_ϕ and σ_ρ are the perturbation standard deviations in the attitude and position, respectively. The standard deviations are chosen from $\|\delta \check{\phi}\| < \delta \phi_{\max}$ and $\|\delta \check{\rho}\| < \delta \rho_{\max}$ such that $\delta \phi_{\max}$ is 10°, 20°, and 45°, and $\delta \rho_{\max}$ is 0.1 m, 0.5 m, and 1 m, for easy, medium, and hard levels, respectively.

For each point-cloud sequence, 30 scan pairs are tested for each perturbation level and scan overlap ratio setting. With 3 point-cloud sequences, 5 scan overlap ratio, and 3 initial perturbation levels, a total of 1350 trials were conducted over 8 different RLF candidates. ICP experiment settings are given in Table II.

Furthermore, the association error is defined as the point-to-plane error [16]. However, the distribution of point-to-point error [17] is used to compute the shape parameters for the

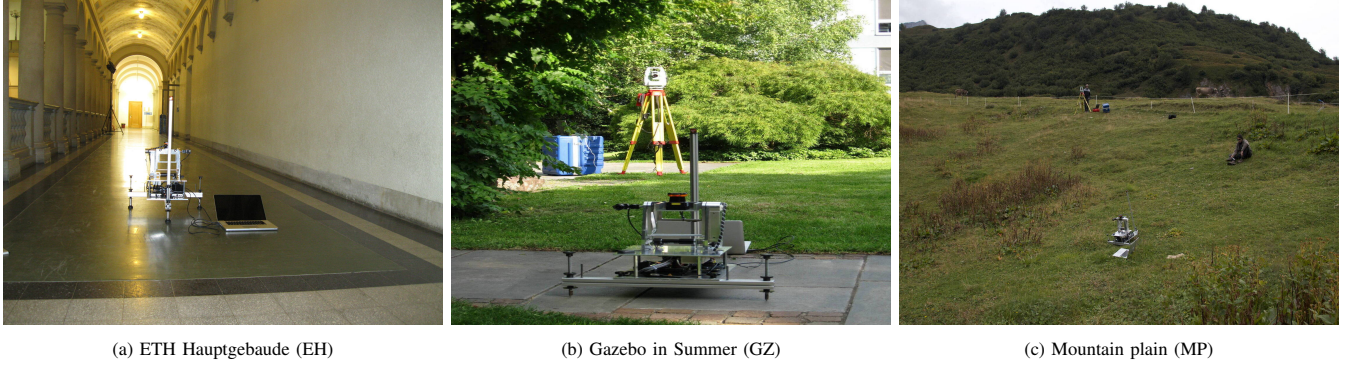


Fig. 2: Contextual photographs of different environments [14].

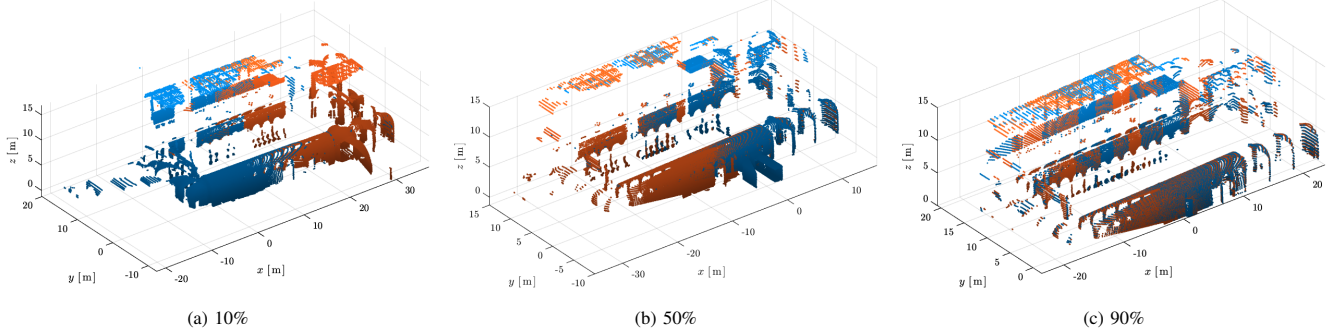


Fig. 3: Three point-cloud scan pairs at different overlap ratio from ETH Hauptgebäude dataset.

TABLE II: ICP experiment settings.

Downsample	VoxelGrid with 10 cm voxel size
Normals	15 nearest neighbours
Point association	Single nearest neighbour
Residual	Point-to-plane error
Convergence	$\ \delta\phi^*\ < 1 \times 10^{-3}$ rad
	$\ \delta\rho^*\ < 1 \times 10^{-3}$ m
Maximum iterations	50

adaptive RLFs such that the distance between two associated points is considered when rejecting outlier matches. The point-to-point error and its squared Mahalanobis are defined as

$$\mathbf{e}_i = \mathbf{r}_{\ell_1}^{p_i s_1} - (\mathbf{C}_{\ell_1 \ell_2} \mathbf{r}_{\ell_2}^{q_i s_2} + \mathbf{r}_{\ell_1}^{s_2 s_1}), \quad (43)$$

$$\epsilon_i^2 = \mathbf{e}_i^\top \Sigma_i^{-1} \mathbf{e}_i, \quad (44)$$

where $\Sigma_i = \mathbf{C}_{\ell_1 \ell_2} \mathbf{R}_{p_i} \mathbf{C}_{\ell_1 \ell_2}^\top + \mathbf{R}_{q_i}$ is the covariance matrix of the i -th point-to-point error, computed using \mathbf{R}_{p_i} and \mathbf{R}_{q_i} , the covariance on the measured points p_i and q_i , respectively. The covariance of p_i is set to $\mathbf{R}_{p_i} = \mathbf{R}_{q_i} = \sigma_\ell^2 \mathbf{1}$, where $\sigma_\ell = 3$ cm as reported in [14].

2) *ICP Alignment Errors*: Table III shows the ICP alignment errors and timing results for each dataset and difficulty combinations. In general, GNC-incorporated methods outperform the baseline methods in terms of alignment errors, especially in more challenging environments, confirming that GNC allows the optimization to better converge without a priori knowledge of the state at the cost of processing time. Amongst GNC-incorporated methods, AGNC and GNC-AMB

outperform GNC-TLS as they can adapt to the residual distribution.

Also, AGNC and AMB take 9-fold less time to converge than GNC-TLS. The difference in time comes from the GNC convergence criteria. GNC-TLS in [8] is formulated such that the original function is retrieved as $\mu \rightarrow \infty$. Thus, GNC-TLS is converged only when the weights are binary, which requires more GNC iterations. On the other hand, the proposed methods retrieve the original function when $\mu \rightarrow 1$.

The proposed GNC-AMB loss function yields the lowest median errors in most of the dataset. The performance difference is more pronounced with more unstructured datasets and with larger initial perturbations. For example, in the case of GZ dataset and hard initial perturbation (GZ-hard), the median rotation and translation errors for GNC AMB are 0.58° and 2.8 cm whereas the runner-up amongst the GNC-enhanced methods, AGNC, yields 1.63° and 15.4 cm.

In addition, the proposed method shows a reduction in variance. For instance, in the experiment with the most unstructured “mountain plain” dataset and with the largest initial perturbation (MP-hard), 75% of translation errors for GNC-AMB are below 9.08 cm compared to the closest contender GNC-TLS with 21.5 cm. A similar pattern is shown in the rotation errors, as the 75th percentile of MP-hard trial is 0.64° for GNC-AMB and 2.48° for AGNC. The improvement in variance reduction in the proposed method is shown in detail in Figure 4.

Notably, amongst the non-GNC methods, AMB performs the closest to the GNC-incorporated methods in terms of the median error, and the variance of AMB is also seen to be

TABLE III: ICP alignment errors and timing results for the environments studied using different RLFs. Median errors are reported for non-GNC methods, while 50%-75% percentiles are reported for the GNC-incorporated RLFs. Amongst GNC-incorporated RLFs, the lowest error in “hard” difficulty for each percentile is highlighted in bold.

Metric	Dataset	Difficulty	Cauchy	Welsch	BA	CA	AMB	GNC-TLS	AGNC	GNC-AMB
$\ \delta\hat{\phi}\ $ [deg]	EH	Easy	0.15	0.15	0.15	0.15	0.15	0.15-0.22	0.15-0.22	0.15-0.22
		Medium	0.14	0.16	0.14	0.14	0.14	0.14-0.23	0.14-0.23	0.14-0.22
		Hard	0.15	16.6	0.15	12.9	0.17	0.16-0.22	0.15-0.21	0.15-0.21
	GZ	Easy	0.37	0.40	0.37	0.37	0.35	0.36-0.49	0.40-0.92	0.36-0.55
		Medium	0.39	5.60	0.39	0.63	0.37	0.38-0.77	0.42-6.73	0.36-0.71
		Hard	2.81	18.3	2.81	17.1	0.77	5.26-20.5	1.63-21.4	0.58-20.1
	MP	Easy	0.30	0.29	0.30	0.26	0.27	0.26-0.38	0.36-1.02	0.29-0.44
		Medium	0.42	1.19	0.42	0.37	0.30	0.31-0.43	0.44-4.08	0.32-0.52
		Hard	0.53	7.09	0.53	1.96	0.42	0.41-3.95	0.42-2.48	0.35-0.64
$\ \delta\hat{\rho}\ $ [cm]	EH	Easy	1.71	2.12	1.71	1.87	1.82	1.92-2.82	1.77-2.77	1.81-2.73
		Medium	1.66	2.10	1.66	1.78	1.75	1.78-2.69	1.73-2.64	1.74-2.65
		Hard	1.91	21.1	1.91	17.8	2.10	2.01-3.09	1.87-2.89	1.93-2.82
	GZ	Easy	1.46	1.66	1.46	1.43	1.51	1.53-2.48	1.53-8.11	1.56-2.77
		Medium	1.86	10.7	1.86	2.80	1.74	1.83-3.72	1.98-59.8	1.68-3.34
		Hard	17.4	34.6	17.4	32.5	4.15	12.0-60.9	15.4-120.	2.80-84.7
	MP	Easy	3.21	3.25	3.21	2.93	3.23	3.29-4.79	3.79-15.1	3.59-6.33
		Medium	3.92	8.18	3.92	4.15	3.51	3.47-5.74	4.53-55.1	3.91-7.60
		Hard	6.75	28.4	6.75	17.2	5.22	4.69-21.5	4.34-37.9	4.03-9.08
Iterations	ALL	ALL	19	40	19	28	17	8	9	9
Time [s]	ALL	ALL	0.87	0.92	1.36	1.38	1.19	33.3	3.86	3.77

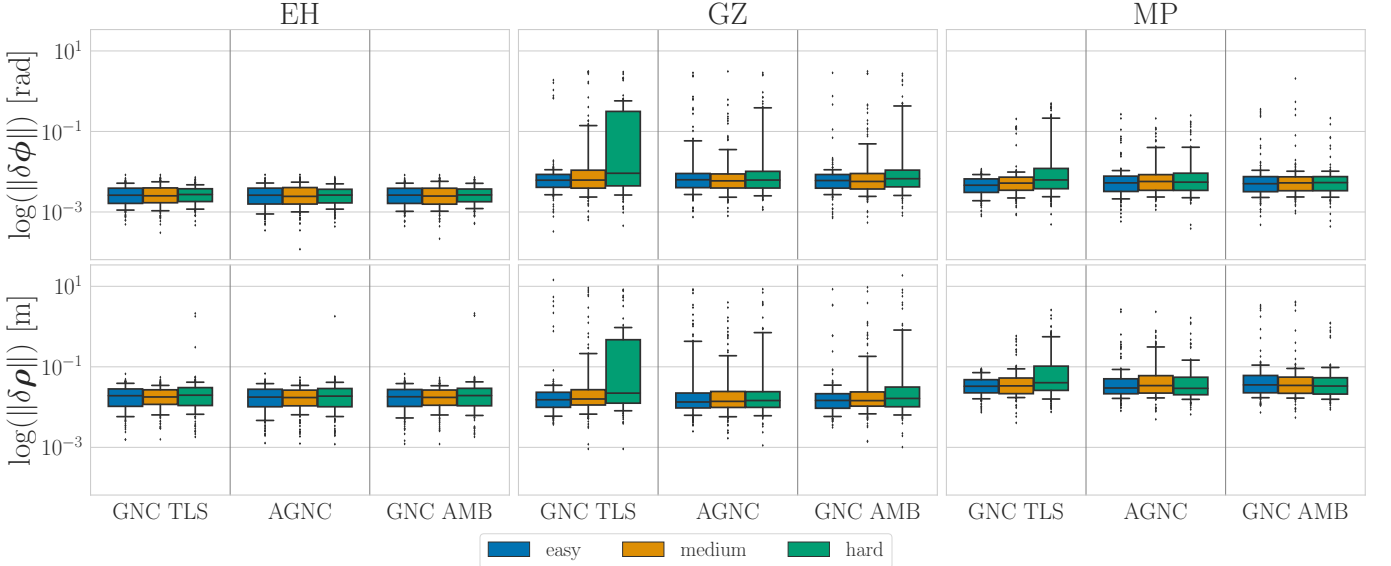


Fig. 4: Box plots show ICP alignment errors for different initial perturbations on a log scale. Only GNC-incorporated methods are shown as they outperform other non-GNC methods as shown in Table III. Boxes represent the middle 50% of the data, with its median shown as a black line. The whiskers represent 10% and 90% percentiles, and the outliers are shown as black dots.

significantly lower than other non-GNC counterparts. Amongst the GNC methods, both the median and variance of alignment errors are lower for GNC-AMB than other GNC contenders. This shows that deriving a loss function based on a Chi distribution is critical for weighting the residuals and rejecting outliers.

3) *Overlap Ratio*: Outlier measurements are often found when the amount of overlap between a scan pair is low. Figure 5 shows that with higher percent overlap, the performance of all RLFs in ICP algorithm improves. GNC-TLS outperforms all other methods in high overlap scenarios, but

the performance of GNC-AMB is comparable to GNC-TLS in low overlap scenarios with significantly lower processing time.

4) *ICP Success Rate*: ICP is considered to have converged when the incremental update $\delta\xi^*$ is less than the convergence thresholds before the maximum number of iterations, both defined in Table II. However, each trial is considered “successful” when both posterior errors, $\delta\hat{\phi}$ and $\delta\hat{\rho}$, are less than the initial perturbations, and the total number of iterations is less than the maximum threshold specified in Table II. The top plot of Figure 6 shows the convergence rate of each

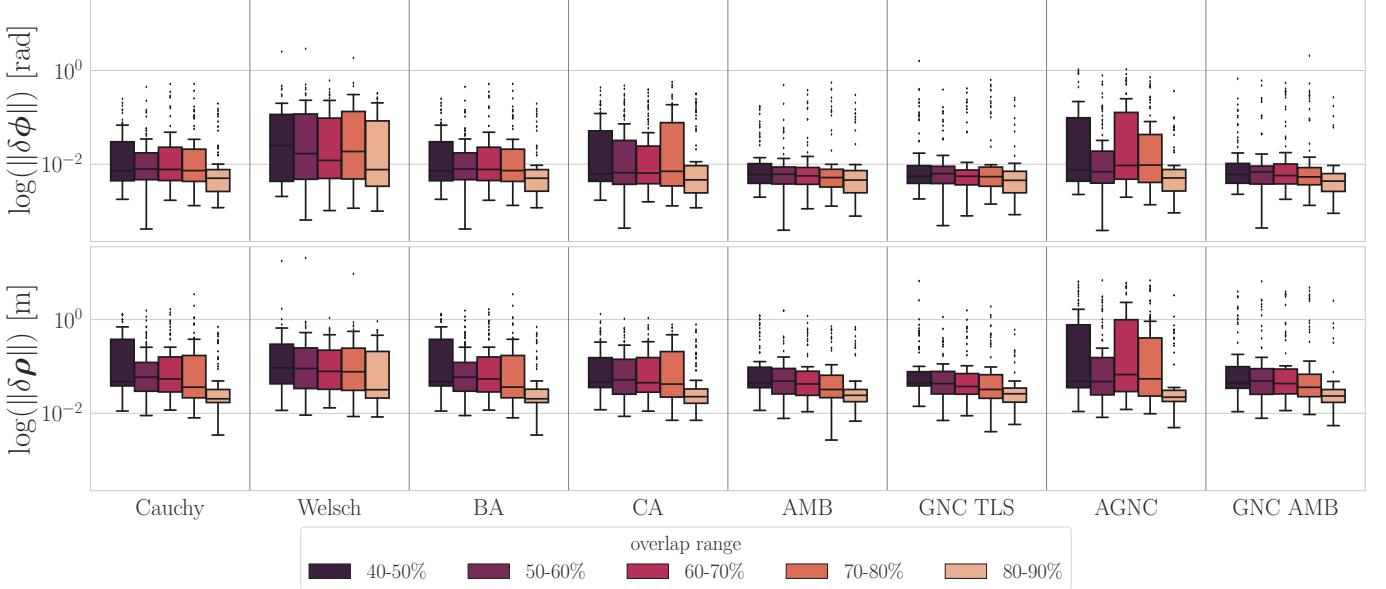


Fig. 5: Box plots show ICP alignment errors for different percent overlaps on a log scale. Only the MP dataset is shown as other datasets show a similar pattern. Boxes represent the middle 50% of the data, with its median shown as a black line. The whiskers represent 10% and 90% percentiles, and the outliers are shown as black dots.

method at different difficulty levels, whereas the bottom figure shows the success rate. The success rate for the “easy” initial perturbations performs worse than medium difficulty because the initial perturbation in the easy case is small, and the posterior ICP estimate is not significantly different from the prior as shown in Figure 7. For medium and hard difficulty levels, GNC-TLS outperforms other methods followed by the proposed method GNC-AMB. The method with the highest percent convergence and success rate are shown in bold for each difficulty level in Figure 6.

Figure 8 shows the number of iterations and convergence time of the successful ICP trials in a log scale. Note that this study was conducted using non-optimized MATLAB code, and timing results are included for relative comparison. Overall, GNC-incorporated methods take fewer iterations but more time to converge than non-GNC methods. Because each ICP least-squares optimization problem is solved gradually from a convex surrogate, each iteration for the GNC-incorporated method takes more time than an iteration of the non-GNC methods.

The non-adaptive RLFs, Cauchy and Welsch, tend to have low convergence time, but also low success rates especially in higher initial perturbations. GNC-TLS, the method that had the highest success rate, requires a significantly longer time to converge, which hinders its practicality in real-time applications. The proposed adaptive GNC methods rival the success rate of GNC-TLS with significantly shorter processing times.

V. CONCLUSION

The adaptive RLF presented in [5] has received ample attention for its adaptability to a wider family of problems and its ability to deal with a larger set of outlier distributions. In this paper, the adaptive RLFs are combined with GNC to solve

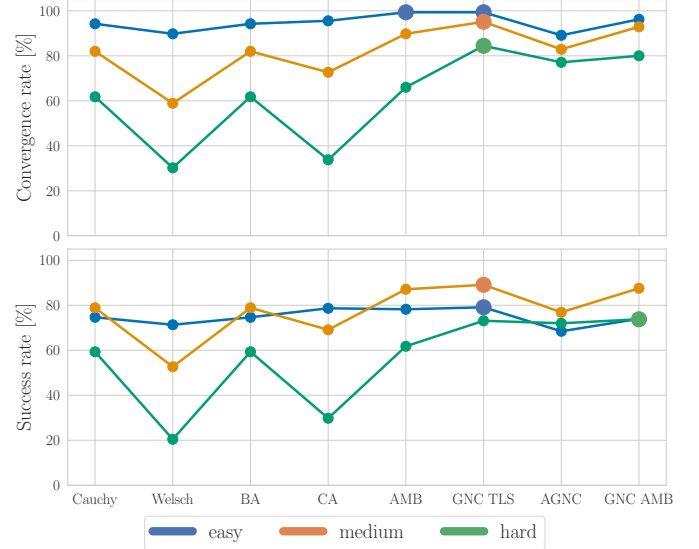


Fig. 6: The percentage of ICP convergence and success for every RLF candidate for various initial perturbations. ICP is considered successful if both the final rotation and translation errors are less than the initial perturbation, $\|\delta\hat{\phi}\| < \|\delta\phi\|$ and $\|\delta\hat{\rho}\| < \|\delta\rho\|$, and the total number of iteration is less than the maximum specified in Table II. The method with the highest percent convergence and success rate are shown in bold for each difficulty level.

least-squares problems, realizing enhanced robustness and convergence properties. Moreover, the Gaussian-like assumption on the residual distribution, which most of the existing loss functions are based on, is replaced by a Chi distribution as proposed by [7] to better represent the underlying residual distribution in multivariate problems. By combining GNC and norm-aware adaptive loss function, the proposed GNC-AMB approach is able to achieve close to the global convergence and reject outliers more effectively at faster rates than other

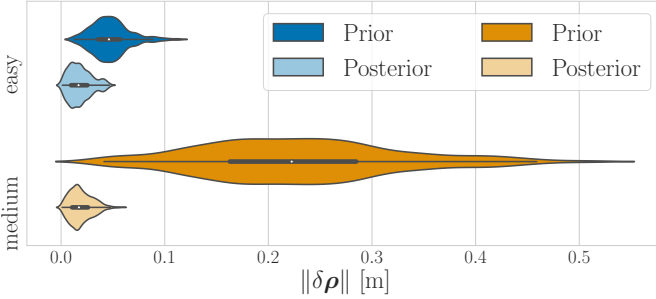


Fig. 7: Prior and posterior translation error distribution for easy and medium difficulty levels for EH dataset.

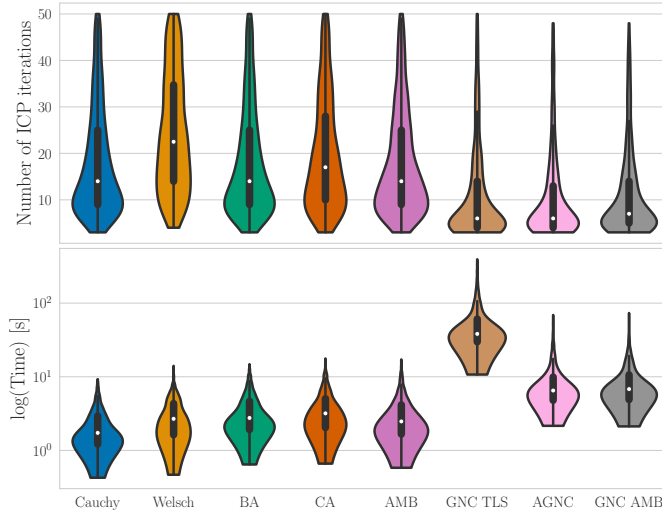


Fig. 8: Violin plots show the number of iterations and convergence time of the successful ICP trials. The times are shown in a log scale for clear representation. The width of each violin distribution is proportional to the number of successful trials.

GNC-based counterparts [8], as well as existing adaptive RLFs [5–7]. The results from linear-regression and PCA problems suggest that this approach is widely applicable to any least-squares problems in state estimation and robotics.

REFERENCES

- [1] C. Cadena, L. Carlone, H. Carrillo, Y. Latif, D. Scaramuzza, J. Neira, I. Reid, and J. J. Leonard, “Past, present, and future of simultaneous localization and mapping: Toward the robust-perception age,” *IEEE Transactions on Robotics*, vol. 32, no. 6, pp. 1309–1332, 2016.
- [2] P. J. Huber, “Robust estimation of a location parameter,” *The Annals of Mathematical Statistics*, vol. 35, no. 1, pp. 73–101, Apr. 1964. [Online]. Available: <http://www.jstor.org/stable/2238020>.
- [3] M. Black and P. Anandan, “The robust estimation of multiple motions: Parametric and piecewise-smooth flow fields,” *Computer Vision and Image Understanding*, vol. 63, pp. 75–104, 1996.
- [4] D. Geman and S. Geman, “Bayesian image analysis,” in *Disordered Systems and Biological Organization*, E. Bienenstock, F. F. Soulié, and G. Weisbuch, Eds., Berlin, Heidelberg: Springer Berlin Heidelberg, 1986, pp. 301–319.
- [5] J. T. Barron, “A general and adaptive robust loss function,” in *IEEE/CVF Computer Society Conference on Computer Vision and Pattern Recognition (CVPR)*, vol. 2019-June, 2019, pp. 4326–4334. arXiv: 1701.03077.
- [6] N. Chebrolu, T. Labe, O. Vysotska, J. Behley, C. Stachniss, T. Läbe, O. Vysotska, J. Behley, and C. Stachniss, “Adaptive robust kernels for non-linear least squares problems,” *IEEE Robotics and Automation Letters*, vol. 6, no. 2, pp. 2240–2247, 2021. arXiv: 2004.14938.
- [7] T. Hitchcox and J. R. Forbes, “Mind the gap: Norm-aware adaptive robust loss for multivariate least-squares problems,” *IEEE Robotics and Automation Letters*, vol. 7, no. 3, pp. 7116–7123, 2022.
- [8] H. Yang, P. Antonante, V. Tzoumas, and L. Carlone, “Graduated non-convexity for robust spatial perception: From non-minimal solvers to global outlier rejection,” *IEEE Robotics and Automation Letters*, vol. 5, no. 2, pp. 1127–1134, 2020. arXiv: 1909.08605.
- [9] M. J. Black and A. Rangarajan, “On the unification of line processes, outlier rejection, and robust statistics with applications in early vision,” *International Journal of Computer Vision*, vol. 19, no. 1, pp. 57–91, 1996.
- [10] R. Chartrand and W. Yin, “Iteratively reweighted algorithms for compressive sensing,” in *IEEE International Conference on Acoustics, Speech and Signal Processing*, 2008, pp. 3869–3872.
- [11] A. Blake and A. Zisserman, *Visual Reconstruction*, Sep. 1987. [Online]. Available: <https://doi.org/10.7551/mitpress/7132.001.0001>.
- [12] P. Babin, P. Giguère, and F. Pomerleau, “Analysis of robust functions for registration algorithms,” in *IEEE International Conference on Robotics and Automation (ICRA)*, vol. abs/1810.0, 2019, pp. 1451–1457.
- [13] J. E. Dennis and R. E. Welsch, “Techniques for nonlinear least squares and robust regression,” *Communications in Statistics - Simulation and Computation*, vol. 7, pp. 345–359, 1978.
- [14] F. Pomerleau, M. Liu, F. Colas, and R. Siegwart, “Challenging data sets for point cloud registration algorithms,” *International Journal of Robotics Research*, vol. 31, no. 14, pp. 1705–1711, Dec. 2012.
- [15] J. Arsenault, “Practical considerations and extensions of the invariant extended Kalman filtering framework,” M.Sc. thesis, McGill University, 2020, p. 114.
- [16] Y. Chen and G. Medioni, “Object modeling by registration of multiple range images,” in *IEEE International Conference on Robotics and Automation (ICRA)*, vol. 3, Sacramento, CA: IEEE, 1991, pp. 2724–2729.
- [17] P. J. Besl and N. D. McKay, “A method for registration of 3D shapes,” *IEEE Transactions on Pattern Analysis and Machine Intelligence*, vol. 14, no. 2, pp. 239–256, 1992.

APPENDIX A OUTLIER PROCESS FUNCTION

The analytical outlier process function $\Phi_\rho(\cdot)$ is derived based on the algorithm discussed in [9]. Differentiating the cost function in (6) with respect to w and ϵ respectively yields

$$\frac{\partial \rho(\epsilon)}{\partial w} = \frac{1}{2}\epsilon^2 + \Phi'_\rho(w), \quad (45)$$

$$\frac{\partial \rho(\epsilon)}{\partial \epsilon} = w\epsilon. \quad (46)$$

The expected value of the differentiated cost function is 0. Thus, substituting (46) into (45) and rearranging the terms yields

$$\Phi'_\rho\left(\frac{1}{\epsilon}\frac{\partial \rho(\epsilon)}{\partial \epsilon}\right) = -\frac{1}{2}\epsilon^2. \quad (47)$$

To find Φ_ρ , integrate (47) with respect to ϵ . To do so, first define a function ϕ as

$$\phi\left(\epsilon^2\right) = \rho(\epsilon). \quad (48)$$

Differentiating (48) with respect to ϵ yields

$$2\epsilon\phi'\left(\epsilon^2\right) = \frac{\partial \rho(\epsilon)}{\partial \epsilon}. \quad (49)$$

Thus, (47) can be rewritten as

$$\Phi'_\rho\left(2\phi'\left(\epsilon^2\right)\right) = -\frac{1}{2}\epsilon^2. \quad (50)$$

Assuming that $\phi''(\epsilon^2) \neq 0$, multiplying $\phi''(\epsilon^2)$ on both sides of (50) and integrating with respect to ϵ^2 yields

$$\int_{-\infty}^{\infty} \Phi'_\rho(2\phi'(\epsilon^2)) \phi''(\epsilon^2) d\epsilon^2 = \frac{1}{2} \Phi_\rho(2\phi'(\epsilon^2)), \quad (51)$$

$$\int_{-\infty}^{\infty} -\frac{1}{2} \epsilon^2 \phi''(\epsilon^2) d\epsilon^2 = -\frac{1}{2} \epsilon^2 \phi'(\epsilon^2) + \frac{1}{2} \phi(\epsilon^2). \quad (52)$$

Equating (51) and (52) results

$$\Phi_\rho(2\phi'(\epsilon^2)) = -\epsilon^2 \phi'(\epsilon^2) + \phi(\epsilon^2). \quad (53)$$

The outlier process function is yet expressed as a function of w . Note that equating (46) and (49) gives

$$2\phi'(\epsilon^2) = w, \quad (54)$$

$$\epsilon^2 = \phi'^{-1}(\frac{1}{2}w). \quad (55)$$

Then, the outlier process function $\Phi_\rho(w)$ can be recovered by substituting (54) and (55) into (53),

$$\Phi_\rho(w) = \phi(\phi'^{-1}(\frac{1}{2}w)) - \frac{1}{2}w\phi'^{-1}(\frac{1}{2}w). \quad (56)$$

Notice that w is defined in terms of $\phi'(\cdot)$ in (54). As w varies between 0 and 1,

$$\lim_{\epsilon \rightarrow 0} \phi'(\epsilon^2) = \frac{1}{2}, \quad (57)$$

$$\lim_{\epsilon \rightarrow \infty} \phi'(\epsilon^2) = 0, \quad (58)$$

must be satisfied. Also, to ensure that a minimum of (6) exists, $\Phi''(w) > 0$. Differentiating (50) with respect to ϵ yields

$$4\Phi''_\rho(2\phi'(\epsilon^2)) \phi''(\epsilon^2) \epsilon = -\epsilon, \quad (59)$$

$$\Phi''_\rho(2\phi'(\epsilon^2)) = -\frac{1}{4\phi''(\epsilon^2)} > 0. \quad (60)$$

Thus, $\phi''(\cdot)$ must be strictly negative, which satisfies the assumption necessary to derive (51) and (52).

APPENDIX B AMB LOSS FUNCTION

The optimal weights derived from the AMB method described in (23) can be rewritten as

$$\tilde{w} = \begin{cases} 1 & \text{if } \epsilon \leq \tilde{\epsilon} \text{ or } \alpha^* = 2, \\ \frac{2}{(\epsilon - \tilde{\epsilon})^2 + 1} & \text{if } \epsilon > \tilde{\epsilon} \text{ and } \alpha^* = 0, \\ \exp(-\frac{1}{2}(\epsilon - \tilde{\epsilon})^2) & \text{if } \epsilon > \tilde{\epsilon} \text{ and } \alpha^* = -\infty, \\ \left(\frac{(\epsilon - \tilde{\epsilon})^2}{|\alpha^* - 2|} + 1\right)^{\alpha^*/2 - 1} & \text{if } \epsilon > \tilde{\epsilon} \text{ and } \alpha^* \in (-\infty, 2). \end{cases} \quad (61)$$

Recall that the relation between the weights and the RLF is given in (5b). Thus, the gradient of the AMB loss function yield

$$\frac{\partial \rho(\epsilon, \tilde{\epsilon}, \alpha^*)}{\partial \epsilon} = \epsilon \tilde{w}(\epsilon, \tilde{\epsilon}, \alpha^*), \quad (62)$$

and the AMB loss function is just an integral of (62),

$$\rho(\epsilon, \tilde{\epsilon}, \alpha^*) = \int_{-\infty}^{\infty} \frac{\partial \rho(\epsilon, \tilde{\epsilon}, \alpha^*)}{\partial \epsilon} d\epsilon. \quad (63)$$

Unfortunately, there is no simple analytical solution to (63), but the numerically integrated loss function is shown in Figure 9.

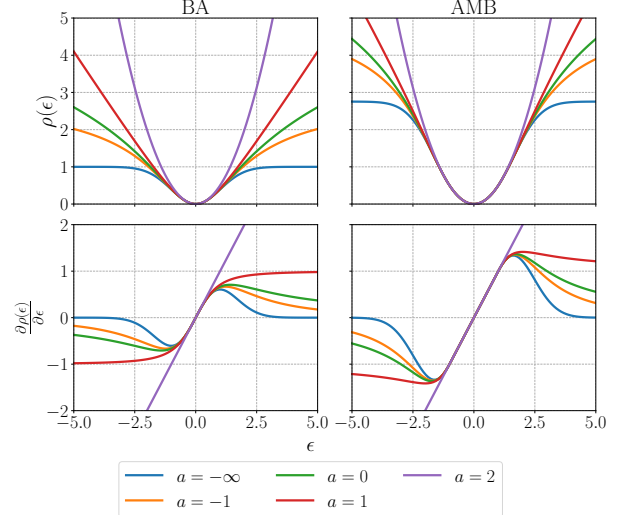


Fig. 9: The general loss function by [5] (BA) and its gradient are shown in the left column for different values of its shape parameter α . The right column shows the AMB loss function and its gradient for the mode $\tilde{\epsilon} = 1$.

APPENDIX C OUTLIER PROCESS FUNCTION FOR AGNC

Recall the surrogate function of (10) is

$$\rho_\mu(\epsilon, \alpha^*) = \frac{|f-2|}{f} \left(\left(\frac{\epsilon^2}{|f-2|} + 1 \right)^{f/2} - 1 \right), \quad (64)$$

where $f = f(\mu, \alpha^*)$ is the shape function. Substituting (64) into (48), differentiating both sides with respect to ϵ , and isolating $\phi'(\cdot)$ results

$$2\epsilon\phi'_\mu(\epsilon^2, \alpha^*) = \rho'_\mu(\epsilon, \alpha^*) \quad (65)$$

$$= \epsilon \left(\frac{\epsilon^2}{|f-2|} + 1 \right)^{f/2-1}, \quad (66)$$

$$\phi'_\mu(\epsilon^2, \alpha^*) = \frac{1}{2} \left(\frac{\epsilon^2}{|f-2|} + 1 \right)^{f/2-1}. \quad (67)$$

Moreover, differentiating ϕ'_μ with respect to ϵ^2 yields

$$\phi''_\mu(\epsilon^2, \alpha^*) = \frac{1}{4} \frac{f-2}{|f-2|} \left(\frac{\epsilon^2}{|f-2|} + 1 \right)^{f/2-2}. \quad (68)$$

Note that the functions in (67) and (68) satisfy the sufficient conditions,

$$\lim_{\epsilon^2 \rightarrow 0} \phi'_\mu(\epsilon^2, \alpha) = \frac{1}{2}, \quad \forall f < 2,$$

$$\lim_{\epsilon^2 \rightarrow \infty} \phi'_\mu(\epsilon^2, \alpha) = 0, \quad \forall f < 2, \quad (69)$$

$$\phi''_\mu(\epsilon^2, \alpha) < 0, \quad \forall f < 2.$$

The inverse function in (55) is

$$(\phi'_\mu)^{-1}(\frac{1}{2}w) = |f-2| \left(w^{2/(f-2)} - 1 \right). \quad (70)$$

Then, the outlier process function can be computed using (56),

$$\Phi_{\rho_\mu} = \frac{|f-2|}{f} \left(w^{f/(f-2)} - 1 \right) - w \frac{|f-2|}{2} \left(w^{2/(f-2)} - 1 \right). \quad (71)$$